RSC Advances

PAPER

View Article Online
View Journal | View Issue

Check for updates

Cite this: *RSC Adv.*, 2018, **8**, 12562

Wet-chemically prepared low-dimensional ZnO/Al_2O_3/Cr_2O_3 nanoparticles for xanthine sensor development using an electrochemical method†

M. M. Alam, *[a] Abdullah M. Asiri,[bc] M. T. Uddin,[a] M. A. Islam[a] and Mohammed M. Rahman [bc]

A reliable xanthine (XNT) chemical sensor was fabricated using a facile wet-chemical method (by co-precipitation) to prepare ZnO/Al_2O_3/Cr_2O_3 nanoparticles (NPs) in an alkaline medium at low temperature. Powder X-ray diffraction (XRD), X-ray photoelectron spectroscopy (XPS), field emission scanning electron microscopy (FESEM), energy-dispersive X-ray spectroscopy (EDS), Fourier transform infrared spectroscopy (FTIR) and ultraviolet-visible spectroscopy (UV-vis) were implemented for detailed characterization of the NPs. To fabricate the working electrode as a XNT chemical sensor probe, a glassy carbon electrode (GCE) with a 0.0316 cm^2 surface area was coated with an ethanolic slurry of the prepared ZnO/Al_2O_3/Cr_2O_3 NPs to make a thin layer and used to analyse XNT in a phosphate buffer system. To evaluate the analytical performances of the XNT chemical sensor, the calibration curve of XNT was plotted as the relationship of current *versus* the concentration of XNT. The plotted calibration curve was found to be linear over the LDR (linear dynamic range) of 0.05 nM to 5.0 μM. The assembled XNT electrochemical sensor exhibited the highest sensitivity (70.8861 $\mu A\ \mu M^{-1}\ cm^{-2}$), the lowest detection limit (1.34 ± 0.07 pM), good reproducibility performance with high accuracy and long-term stability with standard results under ambient conditions. This is a simple route to selectively detect XNT with wet-chemically prepared co-doped ZnO/Al_2O_3/Cr_2O_3 nanomaterials using a reliable electrochemical method at a large scale for safety within healthcare fields.

Received 27th February 2018
Accepted 19th March 2018

DOI: 10.1039/c8ra01734d

rsc.li/rsc-advances

Introduction

Chemically, XNT is known as 3,7-dihydropurine-2,6-dione, and is an intermediate metabolized product of purine in the human body. Therefore, it is found in the human body at concentrations ranging from 0.5–2.5 μM in blood serum and 40–160 μM in urine.[1,2] In the metabolism pathway of purine, XNT is oxidized to uric acid by an enzymatic reaction in the presence of XNT oxides (XOs). For excess XNT levels above the normal range, a number of pathological indicators such as hyperuricemia, tumour hyperthermia, xanthinuria, perinatal asphyxia, pre-eclampsia, leukemia, cerebral ischemia, and gout are recognized in the human body.[3–5] The derivatives of XNT (caffeine and theobromine) are found as mild stimulants in drinks such as coffee and tea. To produce high quality foods, the meat of fresh fish is used in food industries. Due to the degradation of ATP in dead fish, XNT is produced naturally.[6,7] To determine XNT in human serum and food, a reliable and efficient method is needed for safety within the health and food sectors.[8,9] HPLC (high-performance liquid chromatography),[10,11] voltammetric and amperometric,[12,13] and electrophoresis[14] methods are extensively implemented to detect XNT quantitatively in an aqueous medium. In recent years, a number of research activities to detect XNT using electrochemical methods based on various metal oxides and hybrid materials have been reported.[15–18] The aim of this research approach is to develop an electrochemical sensor using an electrochemical method based on ZnO/Al_2O_3/Cr_2O_3 NPs.

ZnO is a semi-conductive oxide with a 3.3 eV band gap energy, a 60 meV exciton binding energy, a high range of resistivity (10^{-3}–10^5 Ω cm) and transparency in the visible wave region.[19–23] Therefore, ZnO shows good optical, electrical and piezo-electrical properties[24,25] and these outstanding properties make ZnO a strong candidate in the field of sensor applications. As a sensor material, ZnO has been applied to detect many toxic chemicals such as acetone,[26] ethanol,[27] 4-aminophenol,[28] and bisphenol A[29] in an aqueous medium. With attractive photo-electronic characteristics, Al_2O_3 has also been applied as a chemical and biological sensor.[30–32] Another active transition

---

[a] *Department of Chemical Engineering and Polymer Science, Shahjalal University of Science and Technology, Sylhet 3100, Bangladesh. E-mail: mmalamsust@gmail.com*

[b] *Chemistry Department, King Abdulaziz University, Faculty of Science, Jeddah 21589, P.O. Box 80203, Saudi Arabia*

[c] *Center of Excellence for Advanced Materials Research (CEAMR), King Abdulaziz University, Jeddah 21589, P.O. Box 80203, Saudi Arabia. E-mail: mmrahman@kau.edu.sa*

† Electronic supplementary information (ESI) available. See DOI: 10.1039/c8ra01734d

metal oxide Cr_2O_3 has also found use in catalysis, wear resistant materials, colorants, and optical and electronic devices.[33–36] Besides this, the binary combination of $ZnO–Al_2O_3$ has found use as a sensor to detect catechol, hydroquinone[37] and methyl violet dye.[38] Moreover, $ZnO–Cr_2O_3$ has been reported as an efficient sensor material to detect ethanol[39] and LPG.[40]

To execute this study, an electrochemical sensor was fabricated by deposition of $ZnO/Al_2O_3/Cr_2O_3$ NPs onto a GCE as a uniform thin layer with the help of a conducting Nafion binder. Thus, the resulting working electrode probe ($ZnO/Al_2O_3/Cr_2O_3$ NPs/binder/GCE) for XNT was implemented to detect XNT in an optimized phosphate buffer system using an electrochemical method under ambient conditions. This research approach might be a reliable and easy method to develop future sensitive chemical and biological sensors based on various doped or undoped ternary metal oxides.

Materials and methodology

Materials and methods

To prepare the ternary metal oxides, analytical grade chemicals such as $Al_2(SO_4)_3 \cdot 18H_2O$, $Zn(NO_3)_2 \cdot 6H_2O$, and $Cr(NO_3)_3 \cdot 9H_2O$ were purchased and used as received. As part of this investigation, various toxins namely 2,4-DNP (2,4-dinitrophenol), 2-APy (2-acetyl pyridine), BC (benzyl chloride), DEM (diethyl malonate), EG (ethylene glycol), *M*-THyd (*M*-tolyl hydrazine hydrochloride), *M*-Xy (*M*-xylol), Zdehy (zimtaldehyde), and XNT were obtained from Sigma-Aldrich (USA). A Thermo-Scientific K-α1 1066 X-ray photoelectron spectroscopy (XPS) instrument with an excitation radiation source (A1 Kα1, beam spot size = 300.0 μm, pass energy = 200.0 eV and pressure ~10^{-8} torr) was used to study the binding energy and oxidation state of the elements existing in the synthesized $ZnO/Al_2O_3/Cr_2O_3$ NPs. To characterize their ability to absorb visible light, the prepared NPs were examined using a Thermo-Scientific 300 UV-vis spectrometer. A Thermo-Scientific NICOLET iS50 (Madison, WI, USA) FTIR spectrometer was used to identify the functional groups in the $ZnO/Al_2O_3/Cr_2O_3$ NPs. The elemental composition and structural morphology were inspected using FESEM analysis equipped with XEDS. The phase crystallinity and particle size of the prepared NPs were evaluated using powder X-ray diffraction (XRD) with an ARL™ X'TRA powder diffractometer. The electrochemical investigation was carried out using a Keithley electrometer (6517A, USA).

Synthesis of the $ZnO/Al_2O_3/Cr_2O_3$ NPs

To synthesise nanomaterials of transition metal oxides, the wet-chemical (co-precipitation process) method is an efficient, conventional method in an alkaline medium with pH 10.5. $Al_2(SO_4)_3 \cdot 18H_2O$, $Zn(NO_3)_2 \cdot 6H_2O$, and $Cr(NO_3)_3 \cdot 9H_2O$ are used

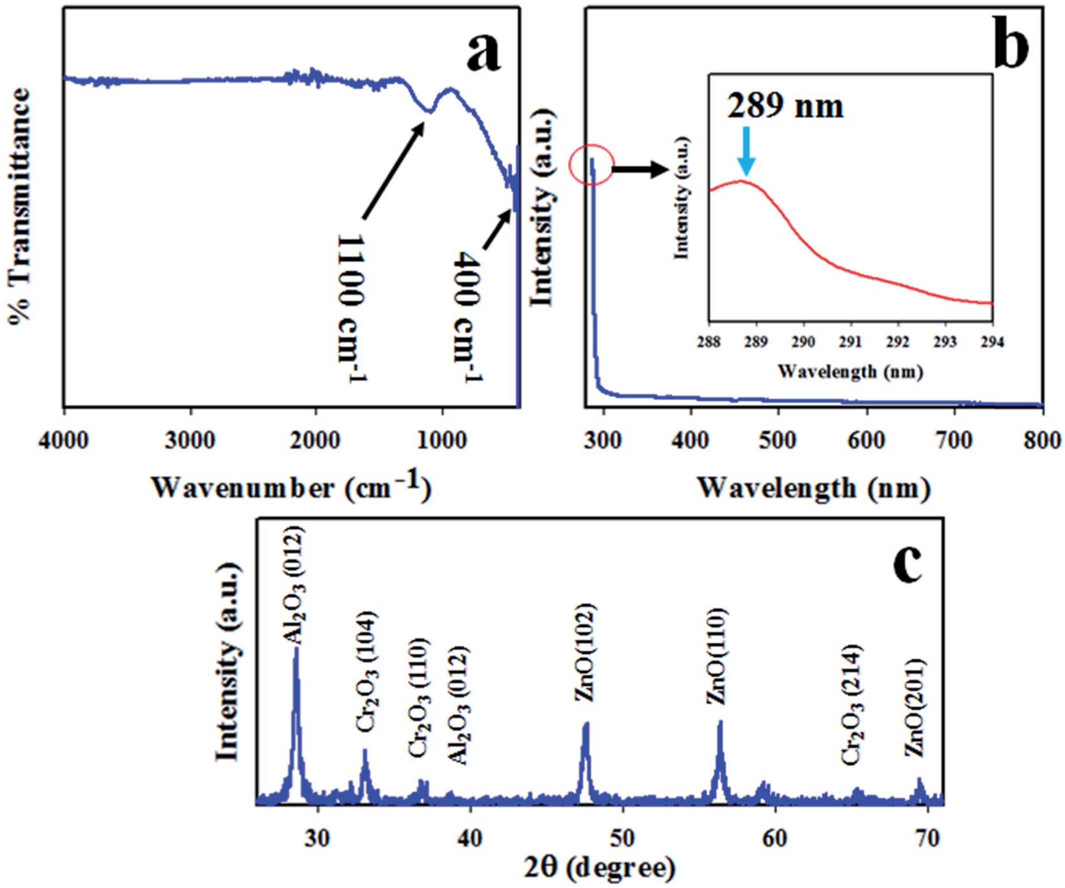

Fig. 1 The optical properties and crystallinity of the synthesized $ZnO/Al_2O_3/Cr_2O_3$ NPs. (a) FTIR analysis, (b) UV-vis spectrum, and (c) phase crystallinity.

to prepare a 0.1 M solution of each salt individually. 100.0 mL round bottom flasks with deionized water and 50.0 mL of each solution in a 250.0 mL conical flask were taken for the synthesis of the doped nanomaterials. Then, the conical flask was put on a hot plate at a temperature of 80 °C with continuous magnetic stirring. Consequently, a prepared 0.1 M NH_4OH solution was added dropwise into the mixture in the conical flask to gradually increase the pH of the solution up to 10.5. Due to the addition of ammonium hydroxide, the pH of the mixture was enriched slowly and the metal ions started to co-precipitate in the form of metal hydroxides and initiated the formation of the nuclei for crystal formation. At pH 10.5, all the metal ions had co-precipitated out quantitatively in the form of a $Zn(OH)_2\cdot Al(OH)_3\cdot Cr(OH)_3\cdot nH_2O$ crystal and with the temperature conditions and magnetic stirring, the process took several hours. A similar process for the formation of nanocrystals in an aqueous medium has been reported earlier.[41–43] The reactions in the conical flask are proposed below:

$$NH_4OH_{(l)} \leftrightarrows NH_{4(aq)}{}^{+} + OH_{(aq)}{}^{-} \qquad \text{(i)}$$

$$Zn(NO_3)_{2(s)} \rightarrow Zn_{(aq)}{}^{2+} + 2NO_{3(aq)}{}^{-} \qquad \text{(ii)}$$

$$Al_2(SO_4)_{3(s)} \rightarrow 2Al_{(aq)}{}^{3+} + 3SO_{4(aq)}{}^{-} \qquad \text{(iii)}$$

$$Cr(NO_3)_{3(s)} \rightarrow Cr_{(aq)}{}^{3+} + 3NO_{3(aq)}{}^{-} \qquad \text{(iv)}$$

$$Zn_{(aq)}{}^{2+} + Al_{(aq)}{}^{3+} + Cr_{(aq)}{}^{3+} + 8OH_{(aq)}{}^{-} \leftrightarrows Zn(OH)_2\cdot Al(OH)_3\cdot Cr(OH)_{3(s)}\downarrow \qquad \text{(v)}$$

Then, the precipitate was separated from the aqueous medium and washed with acetone and deionized water properly. After that, the resultant crystals were kept to dry inside an oven at a temperature of 110 °C overnight. Finally, the dehydrated $Zn(OH)_2\cdot Al(OH)_3\cdot Cr(OH)_{3(s)}$ sample was subjected to calcination at a temperature of 500 °C for 6 hours in a high temperature muffle furnace in the presence of atmospheric oxygen. The metal hydroxides were converted to the metal oxides: $ZnO\cdot Al_2O_3\cdot Cr_2O_3$. The proposed reaction inside the muffle furnace is given as follows:

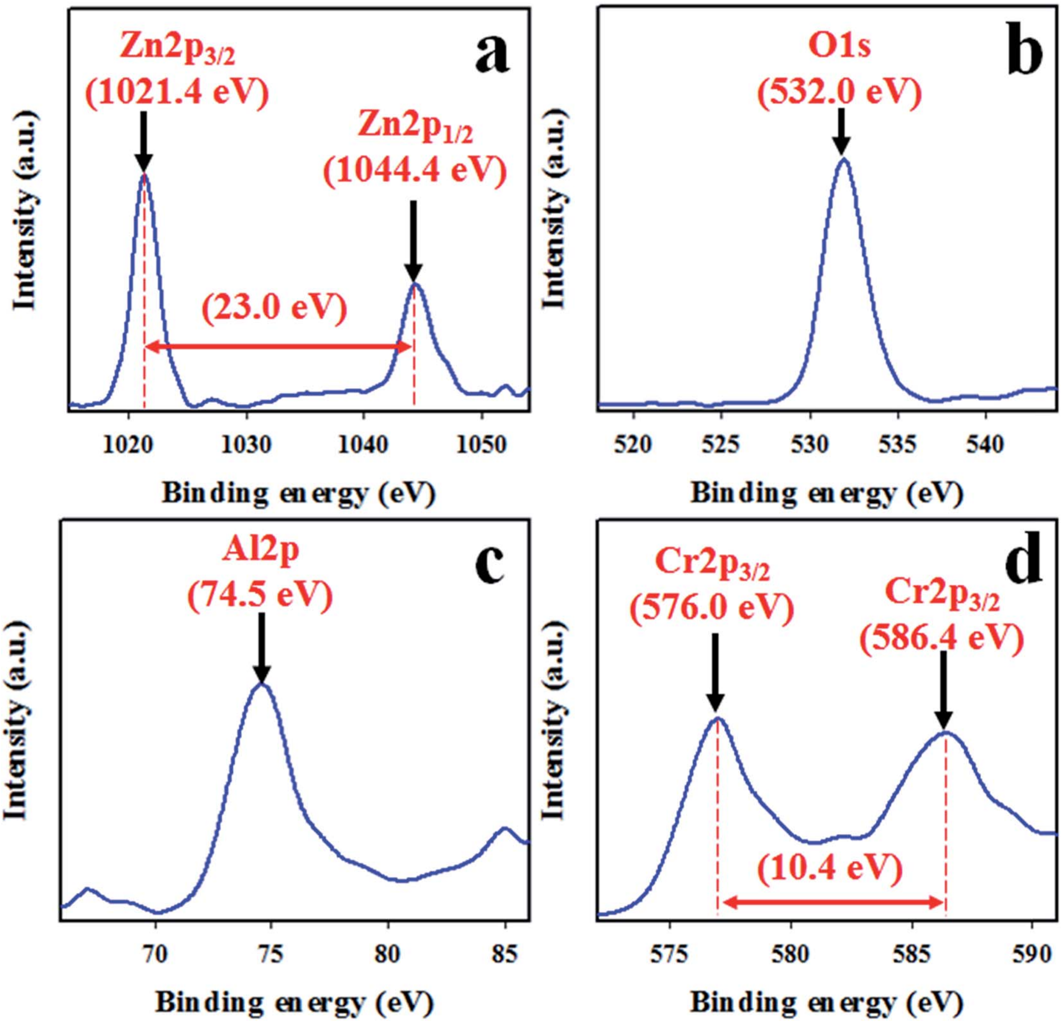

Fig. 2 High resolution XPS spectra of the $ZnO/Al_2O_3/Cr_2O_3$ NPs. (a) The core level XPS spectrum of Zn 2p, (b) O 1s orbitals, (c) Al 2p orbitals, and (d) the 3/2 spin orbitals of Cr 2p.

$$Zn(OH)_2 \cdot 2Al(OH)_3 \cdot 2Cr(OH)_{3(s)} \rightarrow ZnO \cdot Al_2O_3 \cdot Cr_2O_3 + 7H_2O_{(\uparrow)} \quad \text{(vi)}$$

Fabrication of the GCE

The working electrode of the desired sensor was fabricated using a GCE. To do this, the slurry of $ZnO/Al_2O_3/Cr_2O_3$ NPs was prepared in ethanol and deposited onto the glassy carbon electrode in a very uniform thin layer. Then, the modified GCE was kept under ambient conditions for an hour to dry. To improve the binding strength between the NPs and the GCE, a drop of Nafion (5% Nafion suspension in ethanol) was added onto the modified GCE, which was put inside an oven at a temperature of 35 °C for a time adequate to dry the working electrode $ZnO/Al_2O_3/Cr_2O_3$ NPs/binder/GCE entirely. The desired sensor was assembled using an electrometer (a Keithley electrometer), where $ZnO/Al_2O_3/Cr_2O_3$ NPs/binder/GCE acted as working electrode and Pt-wire as a counter electrode. Depending on the concentration, a number of XNT solutions ranging from 0.05 mM to 0.05 nM were prepared and used as target analytes to evaluate the analytical performance of the anticipated XNT sensor. A curve was plotted (known as a calibration curve) as the relationship of current *vs.* the concentration of XNT. From the maximum linearity (r^2) of the calibration curve, the linear dynamic range (LDR) of the projected XNT sensor was estimated. Using the slope of the calibration curve, the sensitivity and detection limit (DL) of the XNT sensor were calculated. During the investigation, the buffer solution in the measuring beaker was kept at a constant 10.0 mL throughout the analysis. The Keithley electrometer was used as a simple two electrode system.

Results and discussion

Optical and structural properties of the $ZnO/Al_2O_3/Cr_2O_3$ NPs

Normally, metal oxides show a characteristic absorption peak in the region 400–800 cm^{-1} in FTIR investigations. To study the FTIR spectrum of the synthesized $ZnO/Al_2O_3/Cr_2O_3$ NPs, FTIR analysis was implemented in the region 400–4000 cm^{-1}. As observed in Fig. 1(a), two major absorption peaks at 400 and 1100 cm^{-1} were exhibited, which are associated with the stretching vibrations of the Zn–O and C–O functional groups, respectively.[44–46] The photocatalytic activity of the $ZnO/Al_2O_3/Cr_2O_3$ NPs was investigated by the implementation of UV-vis analysis in the range of 280–800 nm as shown in Fig. 1(b). As shown in Fig. 1(b), a characteristic absorption band was observed at 289 nm.[47–49] The band gap energy of the $ZnO/Al_2O_3/Cr_2O_3$ NPs was estimated using the following equation and is found to be 4.29 eV:

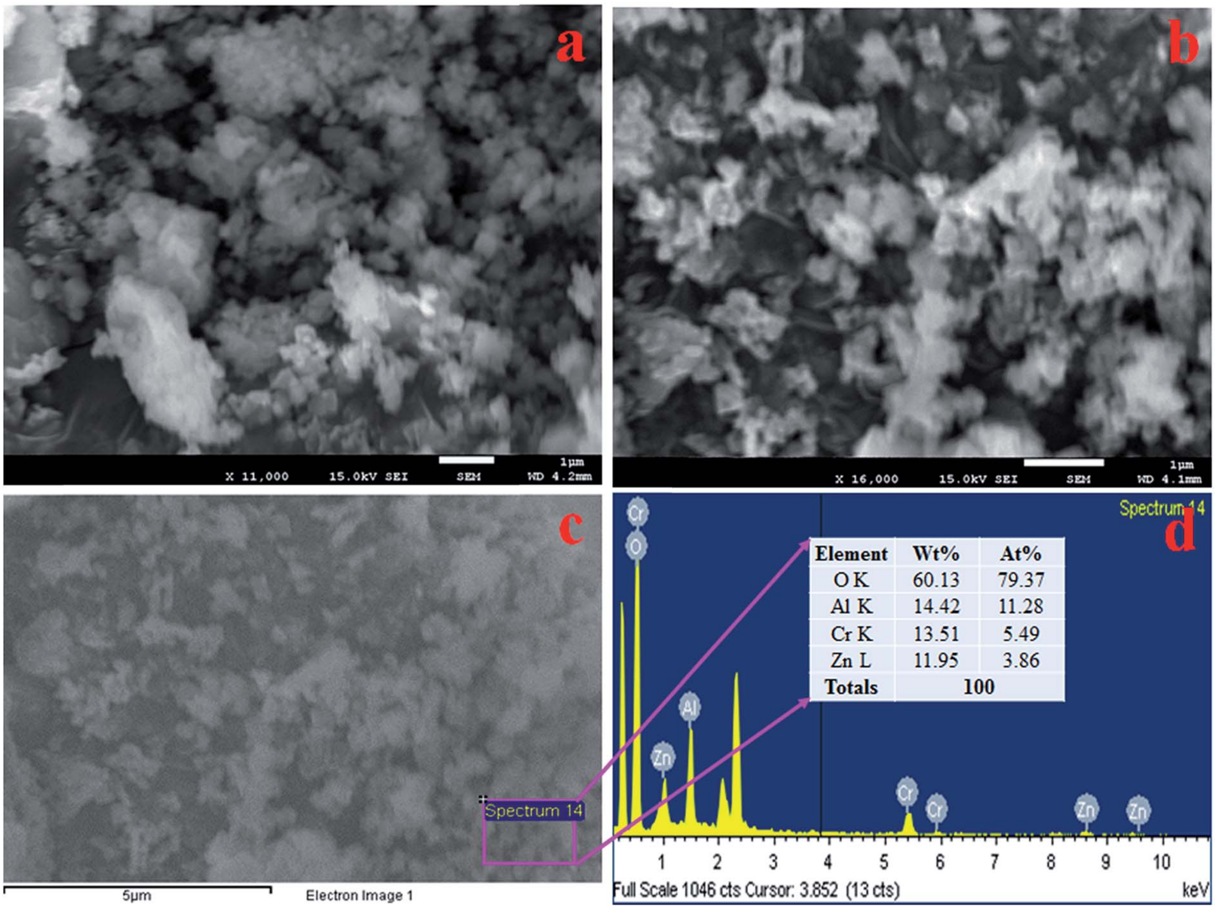

Element	Wt%	At%
O K	60.13	79.37
Al K	14.42	11.28
Cr K	13.51	5.49
Zn L	11.95	3.86
Totals	100	

Fig. 3 Structural and compositional analysis of the prepared $ZnO/Al_2O_3/Cr_2O_3$ NPs. (a and b) Low and high magnification FESEM images and (c and d) elemental analysis with EDS.

$$E_{bg}\ (\text{eV}) = 1240/\lambda \tag{vii}$$

where E_{bg} is the band gap energy and λ is the maximum absorption wavelength.

The crystallinity of $ZnO/Al_2O_3/Cr_2O_3$ NPs was studied by execution of XRD analysis with a radiation source of Cu Kα at 1.5406 ångströms. The resulting XRD pattern recorded over the 2θ range of 26–74° is shown in Fig. 1(c). As shown in Fig. 1(c), the observed peaks of ZnO are shown as (101), (102) and (201) planes, which are indicated by JCPDS no. 00-036-1451 and previous reports of ZnO.[50–52] The diffracted peaks of Cr_2O_3 such as (104), (110), and (214) are also shown in Fig. 1(c) and have great similarity to JCPDS no. 01-089-6744 and those from previous authors.[53,54] Besides this, the reflected XRD peaks (012) and (110) of Al_2O_3 match those of JCPDS no. 077-1716 and reports for Al_2O_3.[55,56] Using the Scherrer equation, the crystal size of the NPs has been estimated from the Al_2O_3 peak (012) and is found to be 22.54 nm.

$$D = 0.9\lambda/(\beta \cos \theta) \tag{viii}$$

where λ is the wavelength of the X-ray radiation (1.5418 Å) and β is the full width at half maximum (FWHM) of the peak at diffracted angle θ.

XPS analysis of the $ZnO/Al_2O_3/Cr_2O_3$ NPs

To measure the surface composition and oxidation state of the synthesized $ZnO/Al_2O_3/Cr_2O_3$ NPs, XPS analysis was performed as shown in Fig. 2. As demonstrated in Fig. 2, the XPS spectra show the peaks associated with Zn, O, Al and Cr only. The other peaks are due to the presence of the impurities. The high resolution XPS spectrum of Zn 2p presented in Fig. 2(a) shows two split spin orbitals centered at 1021.4 eV for Zn $2p_{3/2}$ and 1044.4 eV for Zn $2p_{1/2}$. The spin energy separation is 23.0 eV, which is the characteristic value for the Zn^{2+} oxidation state.[57–59] The O 1s spectrum shows a highly intense peak at 532.0 eV as shown in Fig. 2(b), which can be ascribed to lattice oxygen with an oxidation state of O^{-2} in the $ZnO/Al_2O_3/Cr_2O_3$ NPs.[60,61] As shown in Fig. 2(d), the core level Cr 2p XPS spectrum shows two split spin orbitals at 576.0 eV for Cr $2p_{3/2}$ and 586.4 eV for Cr $2p_{1/2}$ corresponding to the Cr^{3+} oxidation state.[62,63] The XPS peak positioned at

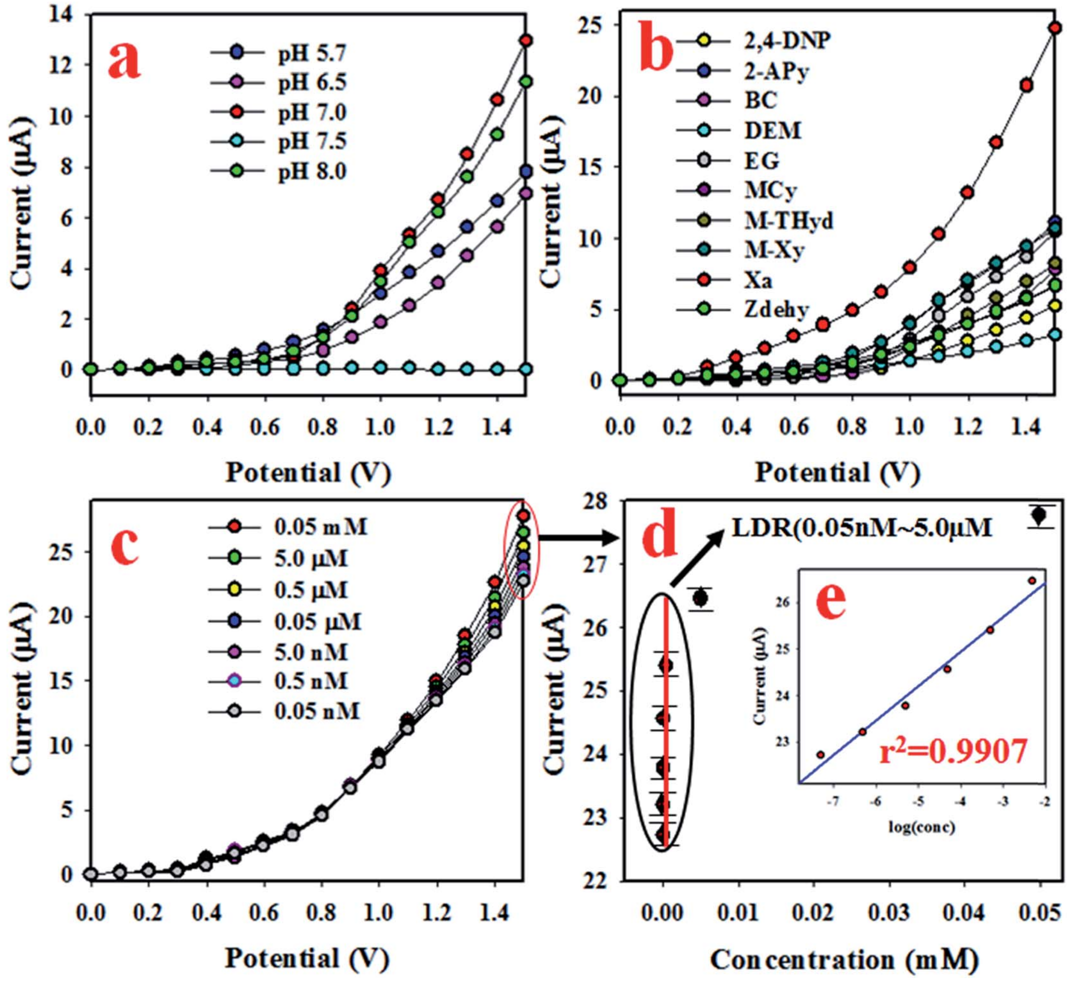

Fig. 4 The estimation of sensor analytical behavior and performance. (a) pH optimization, (b) estimation of the selectivity, (c) concentration variation from lower to higher range, and (d) the calibration curve [inset log(conc.) *vs.* current].

74.5 eV is related to the Al^{3+} state as represented in Fig. 2(c).[64,65]

Morphological and elemental analysis of the $ZnO/Al_2O_3/Cr_2O_3$ NPs

FESEM equipped with EDS was implemented to identify the structural morphology of the synthesized $ZnO/Al_2O_3/Cr_2O_3$ NPs. As demonstrated in Fig. 3(a and b), both the low and high magnification FESEM images confirmed that the prepared $ZnO/Al_2O_3/Cr_2O_3$ oxides are aggregated nanoparticles in shape. An identical result was also observed from EDS analysis as shown in Fig. 3(c and d). The elemental composition of the mixed oxides was found to be 60.13% O, 14.42% Al, 13.51% Cr, and 11.95% Zn and is presented in Fig. 3(d). Therefore, EDS analysis established that the synthesized NPs contained O, Al, Zn, and Cr only and peaks associated with the presence of impurities were not observed.

Analytical performance of the XNT sensor

The synthesized $ZnO/Al_2O_3/Cr_2O_3$ NPs were used to fabricate the desired electrochemical sensor. To assemble the working electrode of this electrochemical sensor, the $ZnO/Al_2O_3/Cr_2O_3$ NPs were deposited onto a GCE as a uniform layer of thin film with a Nafion conducting binder. At the very beginning of this study, the assembled electrochemical (applying the *I–V* method) sensor was tested to find out the most desirable buffer system. To execute this testing, a number of buffer systems with various pH values ranging from 5.7–8.0 were analyzed as shown in Fig. 4(a). As can be observed in Fig. 4(a), the anticipated electrochemical sensor shows the highest *I–V* response at pH 7.0. Therefore, it can be concluded that the proposed sensor based on $ZnO/Al_2O_3/Cr_2O_3$ NPs/binder/GCE has maximum electrochemical activity at pH 7.0. To examine the selectivity of the assembled electrochemical sensor, environmental toxins were analyzed with micro-level concentrations at pH 7.0. The corresponding *I–V* data for 2,4-DNP, 2-APy, BC, DEM, EG, *M*-THyd, *M*-Xy, Zdehy, and XNT are presented in Fig. 4(b), for which the applied potential range of 0 to +1.5 V was used at pH 7.0. Obviously, XNT shows the best *I–V* response among these toxins. To estimate the analytical performance of the XNT electrochemical sensor, it was diluted in deionized water to make up a number of XNT solutions based on concentrations ranging from 0.05 mM to 0.05 nM which were applied as analytes to measure *I–V* responses (Fig. 4(c)). As shown in Fig. 4(c),

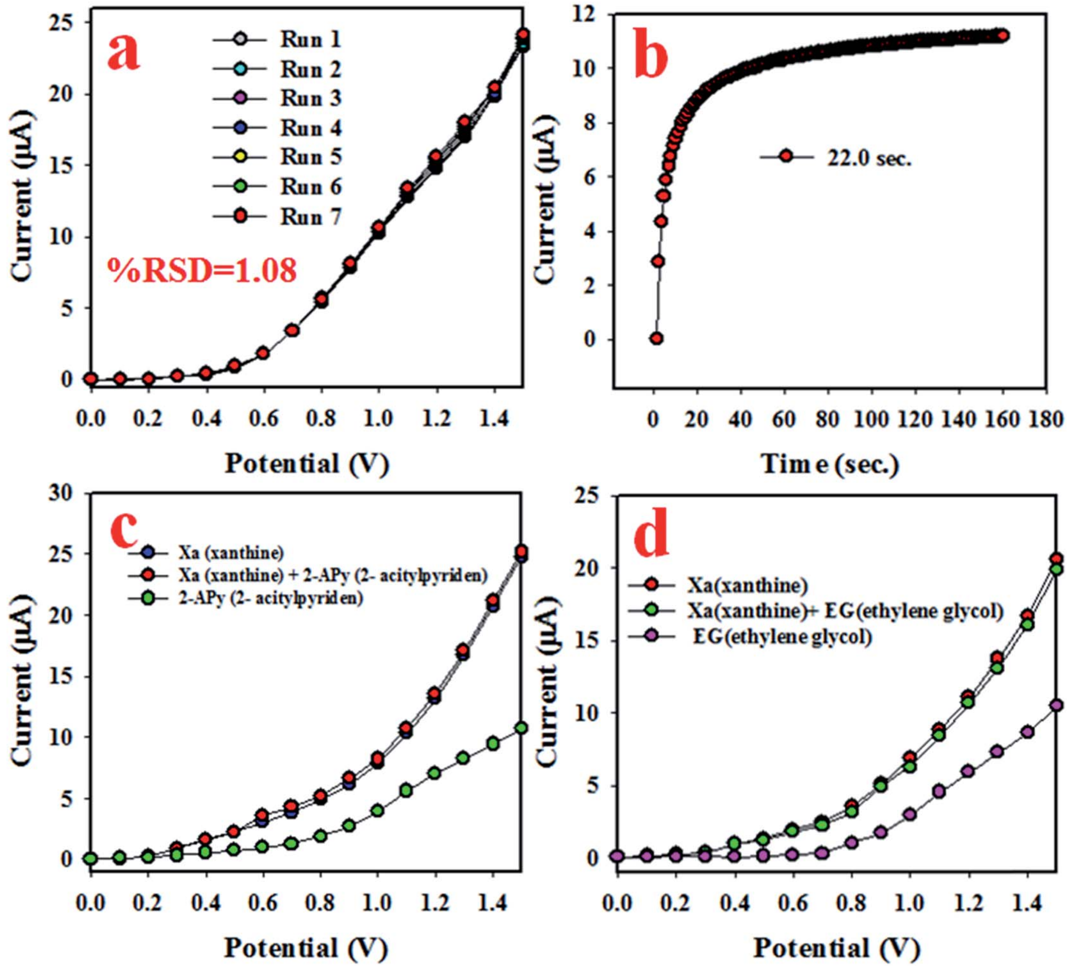

Fig. 5 Reliability investigations of the XNT sensor based on $ZnO/Al_2O_3/Cr_2O_3$ NPs/binder/GCE: (a) testing reproducible performance, (b) response time, and (c and d) interference tests.

the *I–V* responses are distinctive from lower to higher concentration and this performance is observed at applied potentials higher than +1.0 V and at pH 7.0. To plot the calibration curve, the current data at the applied potential +1.5 V were collected from Fig. 4(c) and plotted as concentration of XNT *versus* current as presented in Fig. 4(d). The calibration curve was found to be linear over the concentration range of 0.05 nM to 5.0 μM which was identified as the linear dynamic range (LDR), and basically, this is a wide range of concentrations. The current data for the LDR has been fitted with the regression coefficient value $r^2 = 0.9907$ which provides evidence of the linearity of the calibration curve. As revealed in Fig. 4(d), the current data is consistently scattered lengthways in the plot which provides an indication of the reliability of the analytical method. The sensitivity of the anticipated XNT sensor based on $ZnO/Al_2O_3/Cr_2O_3$ NPs/binder/GCE was assessed from the slope of the calibration curve by considering the active surface area of the GCE (0.0316 cm^2). The value was estimated to be 70.8861 $\mu A\ \mu M^{-1}\ cm^{-2}$. Likewise, the detection limit (DL) was also calculated from the slope of the calibration curve by considering the signal to noise ratio at 3. This obtained the result of 1.34 ± 0.07 pM, which is a significantly lower value than the reported value.

To quantify the capability to reproduce identical electrochemical responses in the optimized buffer system, the proposed XNT electrochemical sensor was used in a reproducibility test. This test was effected with a 5.0 nM concentration of XNT at applied potentials from 0 to +1.5 V. As shown in Fig. 5(a), the seven runs are virtually identical which provides information about the reliability of the XNT sensor. To assess the accuracy of the reproducibility study, the current data were analyzed to estimate the relative standard deviation (RSD) and an excellent RSD was obtained (1.08%). A similar XNT sensor reproducibility test was executed for an elongated period, as shown in Fig. 6. Fig. 6(a–d) shows the equivalent information to Fig. 5(a). Therefore, it can be summarized that the participating XNT sensor is able to significantly detect XNT in real environmental samples. The response time of the sensor is an important criterion to quantify the efficiency. Therefore, the response time of the XNT sensor based on $ZnO/Al_2O_3/Cr_2O_3$ NPs/binder/GCE was calculated using a 5.0 nM concentration of XNT. As revealed in Fig. 5(b), the resulting response time of the XNT sensor is around 22 s, a result which might be considered as having high potential. To confirm the selectivity and interference effect of the XNT sensor, the electrochemical responses

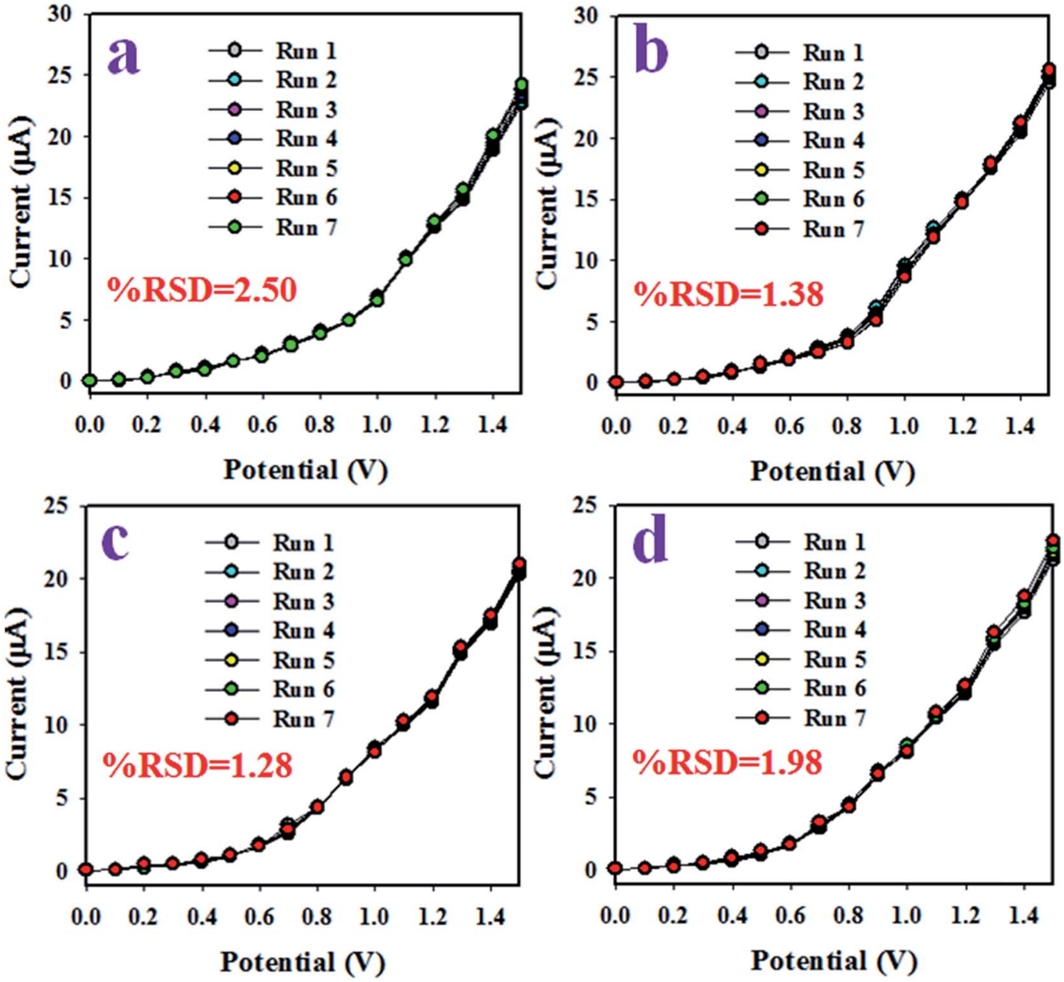

Fig. 6 (a–d) The reproducibility performance for various elongated times (4 days).

Table 1 A comparison of the sensor performance with that of similar work based on different electrode fabrications using an electrochemical approach[a]

Modified GCE	DL	LDR	Sensitivity	Ref.
Co/ZnO NPs/GCE	178.8 pM	5.0 nM to 0.05 mM	53.1 μA μM^{-1} cm^{-2}	66
$ZnO/Al_2O_3/Cr_2O_3$ NPs/GCE	1.34 pM	0.05 nM to 5.0 μM	70.9 μA μM^{-1} cm^{-2}	This work

[a] DL (detection limit) and LDR (linear dynamic range).

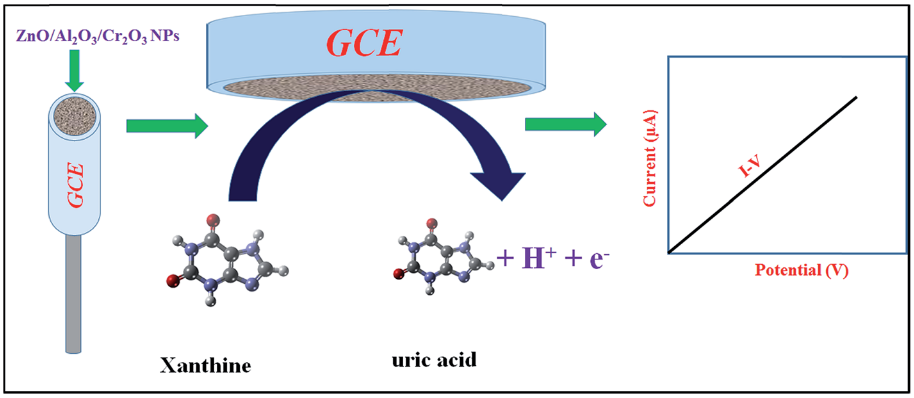

Scheme 1 A prototype representation of the electrochemical oxidation of XNT in an aqueous medium using an electrochemical method.

were investigated as shown in Fig. 5(c and d). It can be summarized that the anticipated XNT sensor is highly selective toward XNT without any interference effects in the presence of other toxins.

As shown in Fig. 4(c), the *I–V* response varies with the corresponding concentration of XNT. The proposed XNT sensor with $ZnO/Al_2O_3/Cr_2O_3$ NPs/binder/GCE was implemented successfully to detect XNT in an optimized phosphate buffer system. A control experiment was performed (Fig. S1†) and is included in the ESI.† Here, a control experiment was performed based on different compositions of fabricated GCEs such as Al_2O_3, ZnO, Cr_2O_3, ZnO/Al_2O_3, Al_2O_3/Cr_2O_3, ZnO/Cr_2O_3, and $ZnO/Al_2O_3/Cr_2O_3$ nanoparticles. Based on these observations, the highest sensor response was exhibited with $ZnO/Al_2O_3/Cr_2O_3$ NPs/binder/GCE compared to those of other fabricated electrodes such as Al_2O_3, ZnO, Cr_2O_3, ZnO/Al_2O_3, Al_2O_3/Cr_2O_3, and ZnO/Cr_2O_3.

During the initial stages of the sensing study of the XNT sensor, the surface coverage on the anticipated working electrode was smaller due to absorption of very few XNT molecules and the corresponding XNT oxidation reaction proceeded. With the increase in XNT concentration in the detecting system, both the surface coverage and rate of reaction increased gradually and approached steady state equilibrium conditions. With further enrichment of the XNT concentration, equilibrium current density was observed in the detecting system. This equilibrium current density is presented in Fig. 4(d) and the current data points are consistently distributed along the linear plot. Therefore, this investigation provides evidence of the reliability of the method. As presented in Fig. 5(b), the response time of the XNT sensor is 22 s and this amount of time is necessary for the XNT sensor to produce a steady state equilibrium *I–V* response. Therefore, the XNT sensor based on $ZnO/Al_2O_3/Cr_2O_3$ NPs/binder/GCE exhibited appreciable analytical performance characteristics such as good sensitivity (70.8861 μA μM^{-1} cm^{-2}), a broad linear dynamic range (0.05 nM to 5.0 μM), a very low detection limit (1.34 ± 0.07 pM), a short response time (22 s), reproducibility with a constant *I–V*

Table 2 Analyses of real environmental samples with the $ZnO/Al_2O_3/Cr_2O_3$ NPs/binder/GCE sensor

Sample	Added XNT concentration (nM)	Measured melamine conc.[a] by $ZnO/Al_2O_3/Cr_2O_3$ NPs/GCE (nM)			Average recovery[b] (%)	RSD[c] (%) ($n = 3$)
		R_1	R_2	R_3		
Industrial effluent	5.000	4.97128	4.96702	4.94034	99.18	0.34
PC-baby bottle	5.000	4.88659	4.92789	4.87152	97.91	0.60
PVC-water bottle	5.000	4.89598	4.93011	4.92118	98.32	0.36
PVC-food packaging bag	5.000	4.95423	4.95025	4.94347	98.99	0.11

[a] Mean of three repeated determinations (signal to noise ratio of 3) with $ZnO/Al_2O_3/Cr_2O_3$ NPs/GCE. [b] The concentration of XNT determined/the concentration taken (unit: nM). [c] Relative standard deviation value indicates precision among three repeated measurements (R_1, R_2, R_3).

response, and high selectivity without interference effects. Also studied was the sensor performance based on various time spans such as intra-day and inter-day validations, which are presented in Fig. 6(a–d). A comparison of the XNT sensor performances was carried out and is included in Table 1. As indicated in Table 1, the XNT sensor based on $ZnO/Al_2O_3/Cr_2O_3$ NPs/binder/GCE shows better performance when comparing the sensitivity, detection limit and linear dynamic range.[66]

Possible sensing mechanism of XNT

During the electrochemical analysis of XNT using the *I–V* method, the XNT molecules are adsorbed onto the surface of the working electrode based on $ZnO/Al_2O_3/Cr_2O_3$ NPs/binder/GCE, where the XNT molecules are oxidized to uric acid (Scheme 1). As illustrated in Scheme 1, due to oxidation of the XNT molecule using the *I–V* method, an electron is produced which is responsible for the higher conductivity of the sensing phosphate buffer medium. A similar pattern of electrochemical oxidation of XNT has been reported previously.[15,16,67]

Validity of the XNT sensor with real environmental samples

To test the validity of the proposed XNT electrochemical sensor based on $ZnO/Al_2O_3/Cr_2O_3$ NPs/binder/GCE, environmental samples such as extracts from a PC-water bottle, a PC-baby bottle, a PVC food packaging bag and industrial effluent have been analyzed using a recovery method. The results of the analyses are presented in Table 2. In Table 2, the obtained results are quite reasonable and acceptable.

Conclusion

The electrochemical sensor was fabricated using wet-chemically prepared $ZnO/Al_2O_3/Cr_2O_3$ nanoparticles and implemented to selectively detect XNT in a phosphate buffer phase. The fabricated sensor shows good sensitivity, a wider linear dynamic range, a much lower detection limit, a quick response time, and excellent reproducibility performance. Besides this, it was found to be stable long-term in a phosphate buffer medium without any interference effects and able to successfully detect XNT in real environmental samples. This has introduced a new route for efficient detection of XNT using an electrochemical approach with ternary $ZnO/Al_2O_3/Cr_2O_3$ nanoparticles for safety within healthcare and biomedical fields.

Conflicts of interest

There are no conflicts to declare.

Acknowledgements

The Center of Excellence for Advanced Materials Research (CEAMR), Chemistry Department, King Abdulaziz University, Jeddah, Saudi Arabia is highly acknowledged for financial support and research facilities.

References

1 R. Boulieu, C. Bory, P. Baltassat and C. Gonnet, Hypoxanthine and xanthine levels determined by high-performance liquid chromatography in plasma, erythrocyte, and urine samples from healthy subjects: the problem of hypoxanthine level evolution as a function of time, *Anal. Biochem.*, 1983, **129**, 398–404.

2 R. Kant, R. Tabassum and B. D. Gupta, Xanthine oxidase functionalized Ta_2O_5 nanostructures as a novel scaffold for highly sensitive SPR based fiber optic xanthine sensor, *Biosens. Bioelectron.*, 2018, **99**, 637–645.

3 P. Kalimuthu, S. Leimkuhler and P. V. Bernhardt, Low-potential amperometric enzyme biosensor for xanthine and hypoxanthine, *Anal. Chem.*, 2012, **84**, 10359–10365.

4 W. Pu, H. Zhao, L. Wu and X. Zhao, A colorimetric method for the determination of xanthine based on the aggregation of gold nanoparticles, *Microchim. Acta*, 2015, **182**, 395–400.

5 S. Yun and L. Jinzhou, Electrochemical sensor using glassy carbon electrode modified with acylpyrazolone-multiwalled carbon nanotube composite film for determination of xanthine, *J. Solid State Electrochem.*, 2012, **16**, 689–695.

6 J. H. T. Luong, K. B. Male and A. L. Nguyen, Application of polarography for monitoring the fish post mortem metabolite transformation, *Enzyme Microb. Technol.*, 1989, **11**, 277–282.

7 D. Shan, Y. Wang, H. Xue and S. Cosnier, Sensitive and selective xanthine amperometric sensors based on calcium carbonate nanoparticles, *Sens. Actuators, B*, 2009, **136**, 510–515.

8 D. Shan, Y. Wang, M. Zhu, H. Xue, S. Cosnier and C. Wang, Development of a high analytical performance-xanthine biosensor based on layered double hydroxides modified-electrode and investigation of the inhibitory effect by allopurinol, *Biosens. Bioelectron.*, 2009, **24**, 1171–1176.

9 D. Shan, Y. Wang, H. Xue and S. Cosnier, Sensitive and selective xanthine amperometric sensors based on calcium carbonate nanoparticles, *Sens. Actuators, B*, 2009, **136**, 510–515.

10 M. Czauderna and J. Kowalczyk, Quantification of allantoin, uric acid, xanthine and hypoxanthine in ovine urine by high-performance liquid chromatography and photodiode array detection, *J. Chromatogr. B: Biomed. Sci. Appl.*, 2000, **744**, 129–138.

11 N. Cooper, R. Khosravan, C. Erdmann, J. Fiene and J. W. Lee, Quantification of uric acid, xanthine and hypoxanthine in human serum by HPLC for pharmacodynamics studies, *J. Chromatogr. B: Anal. Technol. Biomed. Life Sci.*, 2006, **837**, 1–10.

12 U. A. Kirgoz, S. Timur, J. Wang and A. Telefoncu, Xanthine oxidase modified glassy carbon paste electrode, *Electrochem. Commun.*, 2004, **6**, 913–916.

13 J. Pei and X. Y. Li, Xanthine and hypoxanthine sensors based on xanthine oxidase immobilized on a $CuPtCl_6$ chemically modified electrode and liquid chromatography electrochemical detection, *Anal. Chim. Acta*, 2000, **414**, 205–213.

14 T. Richter, L. L. Shultz-Lockyear, R. D. Oleschuk, U. Bilitewski and D. J. Harrison, Bi-enzymatic and capillary electrophoretic analysis of non-fluorescent compounds in microfluidic devices: determination of xanthine, *Sens. Actuators, B*, 2002, **81**, 369–376.

15 R. Devi, S. Yadav and C. S. Pundir, Electrochemical detection of xanthine in fish meat by xanthine oxidase immobilized on carboxylated multiwalled carbon nanotubes/polyaniline composite film, *Biochem. Eng. J.*, 2011, **58–59**, 148–153.

16 S. Z. Baş, H. Gülce and S. Yıldız, Amperometric xanthine biosensors based on electrodeposition of platinum on polyvinylferrocenium coated Pt electrode, *J. Mol. Catal. B: Enzym.*, 2011, **72**, 282–288.

17 R. Devi, S. Yadav and C. S. Pundir, Au-colloids–polypyrrole nanocomposite film based xanthine biosensor, *Colloids Surf., A*, 2012, **394**, 38–45.

18 R. Ojani, A. Alinezhad and Z. Abedi, A highly sensitive electrochemical sensor for simultaneous detection of uric acid, xanthine and hypoxanthine based on poly(L-methionine) modified glassy carbon electrode, *Sens. Actuators, B*, 2013, **188**, 621–630.

19 R. Ayouchi, D. Leinen, F. Martın, M. Gabas, E. Dalchiele and J. R. Ramos-Barradoa, Preparation and characterization of transparent ZnO thin films obtained by spray pyrolysis, *Thin Solid Films*, 2003, **426**, 68–77.

20 R. Romero, M. C. López, D. Leinen, F. Martín and J. R. Ramos-Barrado, Electrical properties of the n-ZnO/c-Si heterojunction prepared by chemical spray pyrolysis, *Mater. Sci. Eng., B*, 2004, **110**, 87–93.

21 H. Zhang, D. Yang, S. Li, X. Ma, Y. Ji, J. Xu and D. Que, Controllable growth of ZnO nanostructures by citric acid assisted hydrothermal process, *Mater. Lett.*, 2005, **59**, 1696–1700.

22 G. Fang, D. Li and B. L. Yao, Fabrication and characterization of transparent conductive ZnO: Al thin films prepared by direct current magnetron sputtering with highly conductive ZnO($ZnAl_2O_4$) ceramic target, *J. Cryst. Growth*, 2003, **247**, 393–400.

23 H. K. Kim, K. S. Lee and H. A. Kang, Characteristics of indium zinc oxide top cathode layers grown by box cathode sputtering for top-emitting organic light-emitting diodes, *J. Electrochem. Soc.*, 2006, **153**, H29–H33.

24 A. Bougrine, A. El Hichou, M. Addou, J. Ebothé, A. Kachouane and M. Troyon, Structural, optical and cathodoluminescence characteristics of undoped and tin-doped ZnO thin films prepared by spray pyrolysis, *Mater. Chem. Phys.*, 2003, **80**, 438–445.

25 A. El Hichou, M. Addou, A. Bougrine, R. Dounia, J. Ebothé, M. Troyon and M. Amrani, Cathodoluminescence properties of undoped and Al-doped ZnO thin films deposited on glass substrate by spray pyrolysis, *Mater. Chem. Phys.*, 2004, **83**, 43–47.

26 M. M. Rahman, M. M. Alam, A. M. Asiri and M. A. Islam, Fabrication of selective chemical sensor with ternary ZnO/SnO_2/Yb_2O_3 nanoparticles, *Talanta*, 2017, **170**, 215–223.

27 M. M. Rahman, M. M. Alam, A. M. Asiri and M. A. Islam, Ethanol sensor development based on ternary-doped metal oxides (CdO/ZnO/Yb_2O_3) nanosheets for environmental safety, *RSC Adv.*, 2017, **7**, 22627–22639.

28 M. M. Rahman, M. M. Alam, A. M. Asiri and M. R. Awual, Fabrication of 4-aminophenol sensor based on hydrothermally prepared ZnO/Yb_2O_3 nanosheets, *New J. Chem.*, 2017, **41**, 9159–9169.

29 M. A. Subhan, P. C. Saha, M. M. Alam, A. M. Asiri, M. Al-Mamund and M. M. Rahman, Development of bis-phenol A sensor based on $Fe_2MoO_4 \cdot Fe_3O_4 \cdot ZnO$ nanoparticles for sustainable environment, *J. Environ. Chem. Eng.*, 2018, **6**, 1396–1403.

30 Z. Jiang, J. Wang, L. Meng, Y. Huang and L. Liu, A highly efficient chemical sensor material for ethanol: Al_2O_3/Graphene nanocomposites fabricated from graphene oxide, *Chem. Commun.*, 2011, **47**, 6350–6352.

31 T. H. Kwon, S. H. Park, J. Y. Ryu and H. H. Choi, Zinc oxide thin film doped with Al_2O_3, TiO_2 and V_2O_5 as sensitive sensor for trimethylamine gas, *Sens. Actuators, B*, 1998, **46**, 75–79.

32 L. M. Hagelsieb, P. E. Lobert, R. Pampin, D. Bourgeois, J. Remacle and D. Flandre, Sensitive DNA electrical detection based on interdigitated Al/Al_2O_3 microelectrodes, *Sens. Actuators, B*, 2004, **98**, 269–274.

33 R. Gupta, E. Mitchell, J. Candler, P. Kahol, K. Ghosh and L. Dong, Facile synthesis and characterization of nanostructured chromium oxide, *Powder Technol.*, 2014, **254**, 78–81.

34 H. Ma, Y. Xu, Z. Rong, X. Cheng, S. Gao, X. Zhang, H. Zhao and L. Huo, Highly toluenesensing performance based on monodispersed Cr_2O_3 porous microspheres, *Sens. Actuators, B*, 2012, **174**, 325–331.

35 S. Inturi, M. Suidan and P. Smirniotis, Influence of synthesis method on leaching of the Cr-TiO_2 catalyst for visible light liquid phase photo-catalysis and their stability, *Appl. Catal., B*, 2015, **180**, 351–361.

36 P. Gibot, F. Schnell and D. Spitzer, $Ca_3(PO_4)_2$ biomaterial: a nontoxic template to prepare highly porous Cr_2O_3, *Mater. Lett.*, 2015, **161**, 172–174.

37 M. Nazari, S. Kashanianb, P. Moradipour and N. Maleki, A novel fabrication of sensor using ZnO-Al_2O_3 ceramic nanofibers to simultaneously detect catechol and hydroquinone, *J. Electroanal. Chem.*, 2018, **812**, 122–131.

38 M. A. Subhan, P. C. Saha, M. M. Rahman, M. A. R. Akand, A. M. Asiri and M. Al-Mamun, Enhanced photocatalytic activity and chemical sensor development based on ternary B_2O_3-$Zn_6Al_2O_9$-ZnO nanomaterials for environmental safety, *New J. Chem.*, 2017, **41**, 7220–7231.

39 W. Wang, Z. Li, W. Zheng, H. Huang, C. Wang and J. Sun, Cr_2O_3-sensitized ZnO electrospun nanofibers based ethanol detectors, *Sens. Actuators, B*, 2010, **143**, 754–758.

40 D. R. Patil and L. A. Patil, Cr_2O_3-modified ZnO thick film resistors as LPG sensors, *Talanta*, 2009, **77**, 1409–1414.

41 M. M. Rahman, M. M. Alam and A. M. Asiri, 2-Nitrophenol sensor-based wet-chemically prepared binary doped Co_3O_4/Al_2O_3 nanosheets by an electrochemical approach, *RSC Adv.*, 2018, **8**, 960–970.

42 M. M. Rahman, M. M. Alam and A. M. Asiri, Sensitive 1,2-dichlorobenzene chemi-sensor development based on solvothermally prepared FeO/CdO nanocubes for environmental safety, *J. Ind. Eng. Chem.*, 2018, DOI: 10.1016/j.jiec.2018.01.019.

43 M. M. Rahman and J. Ahmed, Cd-doped Sb_2O_4 nanostructures modified glassy carbon electrode for efficient detection of melamine by electrochemical approach, *Biosens. Bioelectron.*, 2018, **102**, 631–636.

44 S. J. Salih and A. K. Smail, Synthesis, characterization and evaluation of antibacterial efficacy of zinc oxide nanoparticles, *Pharmaceutical and Biological Evaluations*, 2016, **3**, 3.

45 V. Manoj, M. Karthika, V. S. R. P. Kumar, S. Boomadevi, K. Jeyadheepan, R. K. Karn, R. J. B. Balaguru and S. K. Pandiyan, Synthesis of ZnO nanoparticles using carboxymethyl cellulose hydrogel, *Asian J. Appl. Sci.*, 2014, **7**, 798–803.

46 M. M. AbdElhady, Preparation and Characterization of Chitosan/Zinc Oxide Nanoparticles for Imparting Antimicrobial and UV Protection to Cotton Fabric, *Int. J. Carbohydr. Chem.*, 2012, **2012**, 840591.

47 K. Fooladsaz, M. Negahdary, G. Rahimi, A. H. Tamijani, S. Parsania, H. Akbari-dastjerdi, A. Sayad, A. Jamaleddini, F. Salahi and A. Asadi, Dopamine Determination with a Biosensor Based on Catalase and Modified Carbon Paste Electrode with Zinc Oxide Nanoparticles, *Int. J. Electrochem. Sci.*, 2012, **7**, 9892–9908.

48 R. Srivastava, Investigation on Temperature Sensing of Nanostructured Zinc Oxide Synthesized *via* Oxalate Route, *J. Sens. Technol.*, 2012, **2**, 8–12.

49 M. Noroozi, S. Radiman and A. Zakaria, Influence of Sonication on the Stability and Thermal Properties of Al_2O_3 Nanofluids, *J. Nanomater.*, 2014, 10.

50 M. R. Arefi and S. R. Zarchi, Synthesis of Zinc Oxide Nanoparticles and Their Effect on the Compressive Strength and Setting Time of Self-Compacted Concrete Paste as Cementitious Composites, *Int. J. Mol. Sci.*, 2012, **13**, 4340–4350.

51 A. K. Zak, R. Razali, W. H. A. Majid and M. Darroudi, Synthesis and characterization of a narrow size distribution of zinc oxide nanoparticles, *Int. J. Nanomed.*, 2011, **6**, 1399–1403.

52 Y. Zhang, F. Zhu, J. Zhang and L. Xia, Converting Layered Zinc Acetate Nanobelts To One-Dimensional Structured ZnO Nanoparticle Aggregates and Their Photocatalytic Activity, *Nanoscale Res. Lett.*, 2008, **3**, 201–204.

53 X. Li, Z. Zhang and L. Tao, A novel microarray chemiluminescence method based on chromium oxide nanoparticles catalysis for indirect determination of the explosive triacetone triperoxide at the scene, *Analyst*, 2013, **138**, 1596–1600.

54 L. Farrell, E. Norton, B. J. O'Dowd, D. Caffrey, I. V. Shvets and K. Fleischer, Spray pyrolysis growth of a high figure of merit, nano-crystalline, p-type transparent conducting material at low temperature, *Appl. Phys. Lett.*, 2015, **107**, 031901.

55 S. V. P. Vattikuti and C. Byon, Synthesis and Structural Characterization of Al_2O_3-Coated MoS_2 Spheres for Photocatalysis Applications, *J. Nanomater.*, 2015, 978409.

56 M. H. Zadeh, M. Razavi, O. Mirzaee and R. Ghaderi, Characterization of properties of Al–Al_2O_3 nano-composite synthesized *via* milling and subsequent casting, *J. King Saud Univ., Eng. Sci.*, 2013, **25**, 75–80.

57 D. A. Zatsepin, A. F. Zatsepin, D. W. Boukhvalov, E. Z. Kurmaev, Z. V. Pchelkina and N. V. Gavrilov, Electronic structure and photoluminescence properties of Zn-ion implanted silica glass before and after thermal annealing, *J. Non-Cryst. Solids*, 2016, **432**, 183–188.

58 Y. Cong, D. Han, J. Dong, S. Zhang, X. Zhang and Y. Wang, Fully transparent high performance thin film transistors with bilayer ITO/Al-Sn-Zn-O channel structures fabricated on glass substrate, *Sci. Rep.*, 2017, **7**, 1497.

59 H. Tian, H. Fan, G. Dong, L. Ma and J. Ma, NiO/ZnO p–n heterostructures and their gas sensing properties for reduced operating temperature, *RSC Adv.*, 2016, **6**, 109091–109098.

60 Y. Jung, W. Yang, C. Y. Koo, K. Song and J. Moon, High performance and high stability low temperature aqueous solution-derived Li–Zr co-doped ZnO thin film transistors, *J. Mater. Chem.*, 2012, **22**, 5390–5397.

61 Z. Zulkifli, M. Subramanian, T. Tsuchiya, M. S. Rosmi, P. Ghosh, G. Kalita and M. Tanemur, Highly transparent and conducting C: ZnO thin film for field emission displays, *RSC Adv.*, 2014, **4**, 64763–64770.

62 X. Li, C. He, Y. Bai, B. Ma, G. Wang and H. Tan, Stabilization/solidification on chromium(III) wastes by C3A and C3A hydrated matrix, *J. Hazard. Mater.*, 2014, **268**, 61–67.

63 C. Ruan, K. Xie, L. Yang, B. Ding and Y. Wu, Efficient carbon dioxide electrolysis in a symmetric solid oxide electrolyzer based on nanocatalyst loaded chromate electrodes, *Int. J. Hydrogen Energy*, 2014, **39**, 10338–10348.

64 L. Nie, A. Meng, J. Yu and M. Jaroniec, Hierarchically Macro-Mesoporous Pt/α-Al_2O_3 Composite Microspheres for Efficient Formaldehyde Oxidation at Room Temperature, *Sci. Rep.*, 2013, **3**, 3215.

65 H. Cui, J. Zhou, G. Z. Yang, Y. Sun and C. X. Wang, Growth, modulation and electronic properties of Al_2O_3-coatings SiC nanotubes *via* simple heating evaporation process, *CrystEngComm*, 2011, **13**, 902–906.

66 M. M. Rahman, H. B. Balkhoyor and A. M. Asiri, Ultra-sensitive xanthine sensor development based on wet-chemically prepared Co/ZnO nanoparticles, *Mater. Express*, 2017, **7**, 2.

67 M. Dervisevic, E. Custiuc, E. Çevik, Z. Durmus, M. Şenel and A. Durmus, Electrochemical biosensor based on REGO/Fe_3O_4 bionanocomposite interface for xanthine detection in fish sample, *Food Control*, 2015, **57**, 402–410.